Nano Research

ISSN 1998-0124 CN 11-5974/O4
https://doi.org/10.26599/NR.2026.94909039

Research Article

Chemical vapor transport synthesis of 2D pentagonal $PdSe_2$ with in-plane optical and electrical anisotropy

Haolin Liu[1,§], Jidong Liu[1,§], Di Wu[2], Junzi Li[3], Haibo Gan[1], Zhen He[1], Jiaqi Zhu[4], Yuting Sun[1], Junqi He[1], Tingchao He[3], Qiaoyan Hao[1](✉), Wenjing Zhang[1](✉)

[1] State Key Laboratory of Radio Frequency Heterogeneous Integration, International Collaborative Laboratory of 2D Materials for Optoelectronics Science and Technology of Ministry of Education, Institute of Microscale Optoelectronics, Shenzhen University, Shenzhen 518060, China

[2] College of Electronic Engineering, Huainan Normal University, Huainan 232038, China

[3] Key Laboratory of Optoelectronic Devices and Systems of Ministry of Education and Guangdong Province, College of Physics and Optoelectronic Engineering, Shenzhen University, Shenzhen 518060, China

[4] Institute of Advanced Photonics Technology, Key Laboratory of Photonic Technology for Integrated Sensing and Communication of Ministry of Education, School of Information Engineering, Guangdong University of Technology, Guangzhou 510006, China

[§] Haolin Liu and Jidong Liu contributed equally to this work.

Nano Res., **Just Accepted Manuscript** • https://doi.org/10.26599/NR.2026.94909039

https://www.sciopen.com/journal/1998-0124 on Jul. 18, 2026

TABLE OF CONTENTS (TOC)

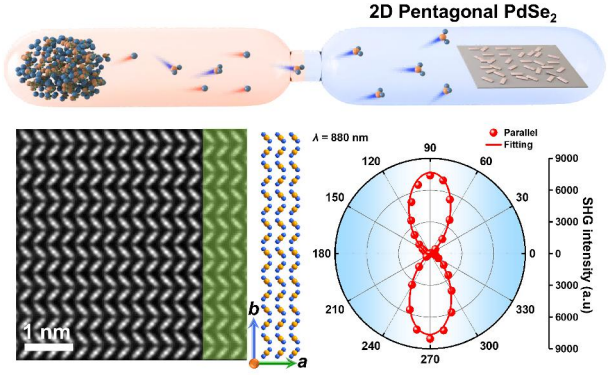

Few-layer and multilayer pentagonal $PdSe_2$ nanosheets were directly grown on sapphire by chemical vapor transport, exhibiting pronounced second-harmonic generation and strong in-plane optical/electrical anisotropy.

Nano Research

Open Access

Research Article

Chemical vapor transport synthesis of 2D pentagonal $PdSe_2$ with in-plane optical and electrical anisotropy

Haolin Liu[1,§], Jidong Liu[1,§], Di Wu[2], Junzi Li[3], Haibo Gan[1], Zhen He[1], Jiaqi Zhu[4], Yuting Sun[1], Junqi He[1], Tingchao He[3], Qiaoyan Hao[1] ✉, and Wenjing Zhang[1] ✉

[1] *State Key Laboratory of Radio Frequency Heterogeneous Integration, International Collaborative Laboratory of 2D Materials for Optoelectronics Science and Technology of Ministry of Education, Institute of Microscale Optoelectronics, Shenzhen University, Shenzhen 518060, China*

[2] *College of Electronic Engineering, Huainan Normal University, Huainan 232038, China*

[3] *Key Laboratory of Optoelectronic Devices and Systems of Ministry of Education and Guangdong Province, College of Physics and Optoelectronic Engineering, Shenzhen University, Shenzhen 518060, China*

[4] *Institute of Advanced Photonics Technology, Key Laboratory of Photonic Technology for Integrated Sensing and Communication of Ministry of Education, School of Information Engineering, Guangdong University of Technology, Guangzhou 510006, China*

[§] *Haolin Liu and Jidong Liu contributed equally to this work.*

Received: 20 April 2026; **Revised:** 1 July 2026; **Accepted:** 18 July 2026

✉ Address correspondence to Qiaoyan Hao, hqy@szu.edu.cn; Wenjing Zhang, wjzhang@szu.edu.cn

Cite this article: *Nano Research*, 2026, 19, 94909039 https://doi.org/10.26599/NR.2026.94909039

ABSTRACT: Two-dimensional (2D) $PdSe_2$ has garnered sustained interest due to its unique puckered pentagonal lattice, which endows it with nonlinear optical activity, strong in-plane anisotropy, sizable bandgap, and environmental stability. However, the advancement of this system toward optoelectronic device applications has been limited by the lack of reliable direct-growth routes for high-quality 2D $PdSe_2$ crystals with regulated thickness. In this paper, we report the bottom-up growth of few-layer and multilayer 2D $PdSe_2$ nanosheets on sapphire substrates via a growth-parameter-regulated chemical vapor transport reaction. The high quality of the as-grown $PdSe_2$ nanosheets is confirmed by aberration-corrected scanning transmission electron microscopy images and low-frequency Raman spectroscopy. We further investigate the strong optical anisotropy of $PdSe_2$ nanosheets using the second-harmonic generation response and angle-resolved polarized Raman spectroscopy. Moreover, electrical transport measurements reveal large anisotropic ratios of 4.9 for electrical conductivity and 6.3 for carrier mobility. This work opens a new route for the synthesis of variable-thickness 2D pentagonal materials and establishes $PdSe_2$ as an excellent candidate for polarization-sensitive optoelectronic devices.

KEYWORDS: chemical vapor transport, pentagonal $PdSe_2$, nonlinear, anisotropy, variable thickness

1 Introduction

Two-dimensional (2D) materials have garnered increasing attention in the fields of nanophotonics and optoelectronics due to their unique physicochemical properties. Unlike conventional isotropic materials such as graphene and MoS_2, which possess highly symmetrical hexagonal lattices, in-plane anisotropic 2D materials exhibit pronounced orientation-dependent optical, electrical, and thermal properties along different crystallographic directions [1, 2]. This anisotropy provides an additional degree of freedom for directional transport of charge and energy, as well as on-demand regulation of device functionality. For instance, owing to their low lattice symmetry, 2D materials like GeSe and NbS_3 demonstrate strong directional dependence in optical and electrical properties, highlighting their potential for polarization-resolved optoelectronic applications [3–6]. Among the emerging anisotropic 2D candidates, pentagonal $PdSe_2$ exhibits a range of intriguing properties, such as a strongly thickness-tunable bandgap (0–1.3 eV) [7], wavelength-tunable linear dichroism [8, 9], excellent air stability [10], and structural reconstruction flexibility [11–13]. These characteristics originate from its unique puckered pentagonal network with strong interlayer coupling and hybridization. Since Xiao et al. first experimentally reported 2D $PdSe_2$ in 2017, tremendous efforts have been devoted to exploring its direct synthesis [14–16], fundamental properties [17, 18], and applications in diverse scenarios [19–21]. For example, Xiao's group grew few-layer $PdSe_2$ crystals with different morphologies and investigated their optical anisotropy and electrical performance [22]. Zhai et al. reported strong in-plane anisotropy and orientation-selective behavior in 2D $PdSe_2$, achieving an anisotropic ratio of electron mobility up to approximately 2.3 at room temperature [8]. More recently, Li et al. studied the layer-dependent second harmonic generation (SHG) polarization responses of $PdSe_2$, revealing distinct differences in SHG polarization orientation and ellipticity

between bilayer and four-layer samples [23]. Beyond these experimental studies, pentagon-based 2D materials have attracted increasing attention because their low-symmetry non-hexagonal lattices can give rise to diverse physical properties, while recent theoretical studies on penta-$PdSe_2$-based systems, including predicted sliding ferroelectricity and a Boson-peak-like hump induced by phonon localization, further highlight the importance of developing reliable direct-growth strategies for high-quality $PdSe_2$ nanosheets and exploring their anisotropic properties [24–26]. To date, studies on the anisotropic properties of $PdSe_2$ have been mainly restricted to mechanically exfoliated few-layer samples and those grown by chemical vapor deposition (CVD) [27–31]. Owing to phase variations and the rich polymorphic nature of $PdSe_2$ [15, 32], the efficient preparation of high-quality 2D $PdSe_2$ with variable thickness remains insufficiently explored and requires further investigation.

Chemical vapor transport (CVT) is a reliable growth method for synthesizing various high-quality bulk single crystals. In recent years, a surge of attention has been directed toward extending this bulk crystal growth method to produce atomically thin 2D materials with crystallinity comparable to that of mechanically exfoliated counterparts. In contrast to conventional CVD growth, which is generally conducted in an open-flow environment, the CVT process proceeds in a vacuum-sealed quartz tube with a controlled temperature gradient and a confined precursor environment. The confined geometry is beneficial for suppressing oxygen-related interference and regulating the transport and crystallization process through the control of growth temperature and precursor amounts [33]. Unlike flux-assisted growth, the CVT route does not rely on an external flux medium and enables direct growth of 2D nanosheets on different substrates. For example, Jiao et al. successfully synthesized a series of isotropic 2D transition metal dichalcogenides, including $TiSe_2$, MoS_2, WS_2, $MoSe_2$, and $PtSe_2$, via CVT by tuning the growth kinetics [34–36]. This approach has also proven effective for producing anisotropic low-dimensional materials with nanoscale thickness, such as red phosphorus (RP) [37], $ReSe_2$ [38], and Te [39]. Qiu et al. employed CVT to grow Ti-doped MoS_2 monolayers and perovskite/MoS_2 vertical heterostructures, demonstrating an effective route for 2D material modification and heterostructure fabrication [40, 41]. Very recently, Duan et al. fabricated centimeter-scale uniform MoS_2 and WS_2 films using an enclosed CVT method at a low temperature (<450 ℃) [42]. These advances suggest that CVT may offer a new strategy for the lateral growth of 2D $PdSe_2$, while the anisotropic properties of the resulting products remain to be explored.

In this work, we report the direct growth of $PdSe_2$ nanosheets via a one-step CVT reaction. By controlling the growth parameters, we successfully synthesized high-crystallinity $PdSe_2$ nanosheets on sapphire substrates, with lateral dimensions up to tens of micrometers and thicknesses down to approximately 4 nm. The as-grown $PdSe_2$ nanosheets exhibited a strong SHG effect under 880 nm excitation. A comprehensive investigation was conducted into the in-plane optical anisotropy of the $PdSe_2$ nanosheets using angle-resolved polarized Raman spectroscopy. Moreover, field-effect transistor devices based on CVT-grown $PdSe_2$ nanosheets exhibited angle-resolved electrical transport properties, with a large anisotropic conductance ratio of 4.9 and an anisotropic mobility ratio of 6.3. This study not only provides a reliable method for the direct synthesis of high-quality 2D pentagonal materials but also offers important insights for exploring the polarization-sensitive functionality of the $PdSe_2$ system.

2 Experimental

2.1 CVT synthesis of 2D $PdSe_2$ crystals

Prior to crystal growth, high-purity Se powders were thoroughly ground and dried in a vacuum oven at 80 °C for ten hours. Stoichiometric (8:1) amounts of Se powder (0.067 g) and PdI_2 powder (0.038 g) were weighed and loaded into a quartz tube at one end inside an Ar-filled glovebox. A double-side polished *c*-plane sapphire substrate was placed at the other end of the quartz tube and separated from the precursors by a neck in the tube. The tube was then connected to a custom-made vacuum isolation valve to avoid air contamination, followed by evacuation and flame-sealing to create an enclosed chamber for subsequent crystal growth. The 15-cm-long sealed tube was loaded into the central hot zone of the furnace, heated to 800–900 °C at a rate of 20 °C min^{-1}, and maintained at this temperature for 1 h. Note that the substrate was positioned 8 cm away from the source materials to establish a temperature gradient of approximately 50 °C, as measured by a thermocouple. After that, the furnace was cooled to 500 °C over 2 h and then rapidly cooled to room temperature by opening the furnace cover. In our experiments, the inner diameter of the necking was fixed at 5 mm, and its position was set at 8 cm from the source materials. The thickness and lateral size of the target products were carefully tuned by controlling experimental conditions, including growth temperature and substrate (Figures S1 and S2).

2.2 Characterization

The morphology and topography of the CVT-grown $PdSe_2$ nanosheets were observed using an optical microscope (Nikon Y-IDP) and AFM (Bruker Dimension ICON system). Raman spectra were collected using a WITec Alpha 300R confocal Raman spectrometer with a 532 nm laser source. The polarization state of the laser was controlled by rotating a half-wave plate in steps of 10°. STEM images were taken using a Cs-corrected TEM (FEI Titan Cubed Themis G2 300) operated at an accelerating voltage of 300 kV. The chemical valence and bonding states of the $PdSe_2$ nanosheets were characterized by XPS (PHI VersaProbe 4, ULVAC PHI) using Al Kα radiation.

2.3 SHG Measurement

The SHG signal was detected in a reflection geometry. Femtosecond laser pulses at wavelengths ranging from 780 to 960 nm, with a repetition rate of 80 MHz and a pulse width of 80 fs (Spectra-Physics Solstice Maitai HP), were used as the excitation source. The laser pulses were focused on the sample using a 50x objective lens with a numerical aperture of 0.8.

2.4 Transfer of CVT-Grown $PdSe_2$ nanosheets

The $PdSe_2$ nanosheets grown by CVT were transferred from the sapphire growth substrate onto a SiO_2/Si substrate using a polymer-assisted wet transfer process. First, a solution of poly(methyl methacrylate) (PMMA, 15 wt%) was spin-coated (500 rpm for 10 s; 3500 rpm for 1 min) on top of the $PdSe_2$ nanosheets and baked on a hotplate at 105 °C for 2 min. The edge of the PMMA film was gently peeled off with tweezers to

facilitate the subsequent etching and removal process. Afterward, the PMMA/$PdSe_2$ stack was released from the sapphire by etching in 1 mol L^{-1} sodium hydroxide aqueous solution at 60 °C for 20 min. The detached PMMA/$PdSe_2$ film was rinsed in deionized water several times and transferred onto the SiO_2/Si substrate. The SiO_2/Si substrate with the PMMA/$PdSe_2$ film was baked on a hotplate at 105 °C for 10 min to dry the sample and enhance adhesion. Finally, the PMMA film was removed by repeatedly immersing the sample in hot acetone (50 °C, 10 min) several times, followed by rinsing with isopropanol and drying under a flow of N_2 gas.

2.5 Device Fabrication and Characterization

Photoresist (AZ 5214-E) was spin-coated (500 rpm for 10 s; 4000 rpm for 1 min) to uniformly cover the SiO_2/Si substrate, followed by baking at 105 °C for 1 min to solidify. The source and drain electrodes were patterned using a laser writer (MicroWriter ML3, Durham Magneto Optics Ltd.). Next, the sample was immersed in the developer solution (AZ 400K) for 40 s and rinsed in deionized water for 20 s. Finally, Ti/Au (10 nm/40 nm) metals were deposited using an electron-beam evaporation system. The electrical transport properties of the samples were measured using a Keithley 4200 semiconductor characterization system connected to a Lakeshore cryogenic probe station under ambient conditions.

3 Results and discussion

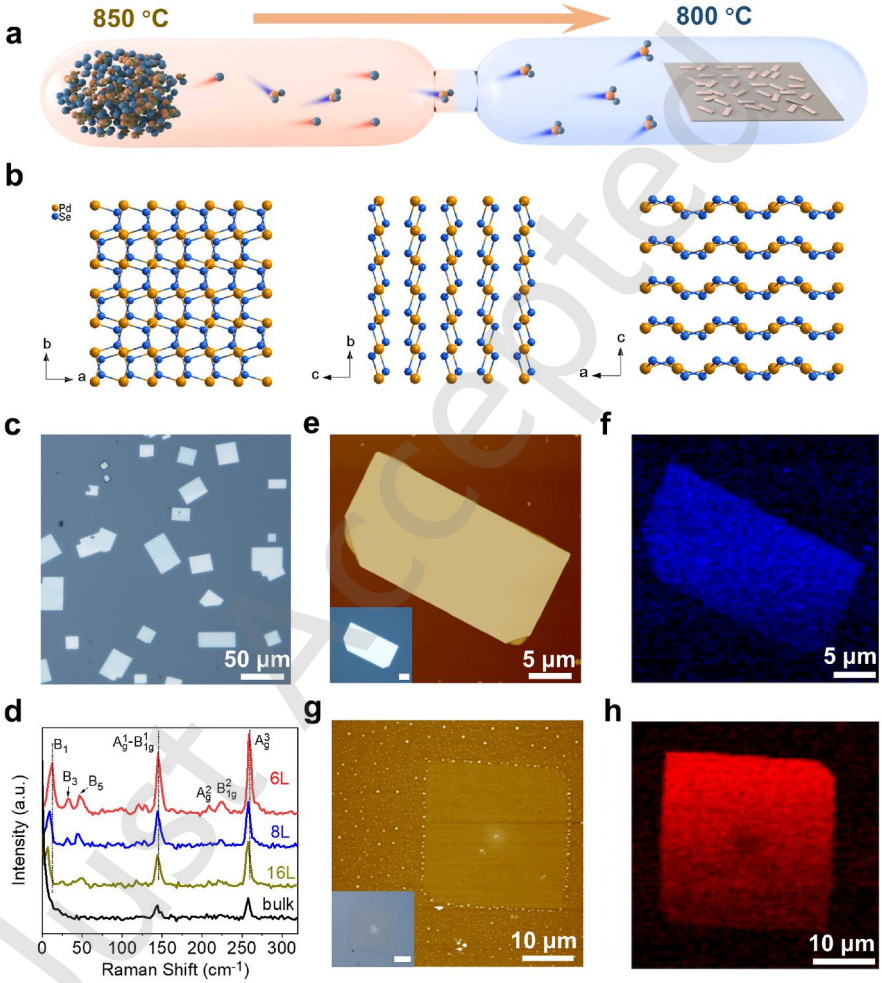

Figure 1. Synthesis and characterization of $PdSe_2$ nanosheets. (a) Schematic illustration of the CVT setup for the growth of 2D $PdSe_2$. (b) Atomic structure of 2D pentagonal $PdSe_2$. (c) Optical microscopy image of as-grown $PdSe_2$ nanosheets on a sapphire substrate. (d) Raman spectra of $PdSe_2$ nanosheets with different thicknesses. (e,f) AFM topography image and Raman mapping of the A_g^3 characteristic peak for a ~35-nm-thick $PdSe_2$ nanosheet. The inset shows the corresponding optical microscopy image (scale bar: 5 μm). (g,h) AFM topography image and Raman mapping of the A_g^3 characteristic peak for a ~5-nm-thick $PdSe_2$ nanosheet. The inset shows the corresponding optical microscopy image (scale bar: 10 μm).

As schematically illustrated in Figure 1a, $PdSe_2$ nanosheets with high crystalline quality were synthesized using a chemical vapor transport (CVT) setup, in which a temperature gradient is established between the source and deposition zones to facilitate the transport of precursors and the epitaxial crystallization of products on the substrate. In this work, we used PdI_2 and Se powder as precursors to produce $PdSe_2$ nanosheets without adding an extra transport agent (see the Experimental Section for details). The orthorhombic lattice of $PdSe_2$ consists of single layers of $PdSe_2$ stacking along the *c*-axis, where each monolayer is composed entirely of pentagonal rings (Figure 1b). In CVT routes, the confined geometry allows for modulation of the reactant partial pressure. By optimizing the growth conditions, including growth temperature and substrate, $PdSe_2$ nanosheets in rectangular shapes were produced on sapphire substrates at a growth temperature of 800 ℃ and a Pd:Se atomic ratio of 1:8. Optical microscopy and atomic force microscopy (AFM) show that the lateral size and thickness of the as-grown $PdSe_2$

nanosheets were mainly in the ranges of 10–50 μm and 4–55 nm, respectively, as shown in Figure 1c and Figures S3–S5. Figure 1d shows the Raman spectra of samples with different thicknesses. The bulk sample, represented by a $PdSe_2$ nanosheet with a thickness of approximately 44 nm, exhibited four distinct Raman peaks at ~143.7, 204.8, 221.1, and 256.8 cm^{-1} in the high-frequency region (>100 cm^{-1}), corresponding to the vibrational modes of A_g^1-B_{1g}^1, A_g^2, B_{1g}^2, and A_g^3, respectively [8]. With decreasing layer number, these four Raman peaks gradually shifted to higher frequencies, indicating strong interlayer interaction in $PdSe_2$ crystals. Furthermore, for few-layer and multilayer $PdSe_2$, the characteristic set of low-frequency (LF) Raman peaks (<60 cm^{-1}) can serve as fingerprints for unambiguous assignment of the layer number. Three representative samples with thicknesses of approximately 4, 5, and 10 nm exhibited prominent LF breathing modes of $PdSe_2$, which can be assigned to layer numbers of 6, 8 and 16, respectively, in good agreement with previous reports [43, 44]. Moreover, the Raman peak positions and spectral features of the typical CVT-grown samples were in good agreement with those of mechanically exfoliated counterparts at comparable thicknesses, confirming that the CVT-grown $PdSe_2$ nanosheets retained the intrinsic layer-dependent vibrational features of pentagonal $PdSe_2$ (Figure S6). Raman intensity mappings of the A_g^3 characteristic peak were further performed on typical samples with thicknesses of about 35 nm and 5 nm (Figures 1e–1h and Figure S7). The uniform distribution indicates the high crystalline quality and spatial uniformity of the as-grown $PdSe_2$ nanosheets. More importantly, the characteristic Raman peaks remained nearly unchanged, without obvious peak shift or intensity attenuation after two months of exposure to ambient air (Figure S8), suggesting good environmental stability of the as-grown $PdSe_2$ nanosheets.

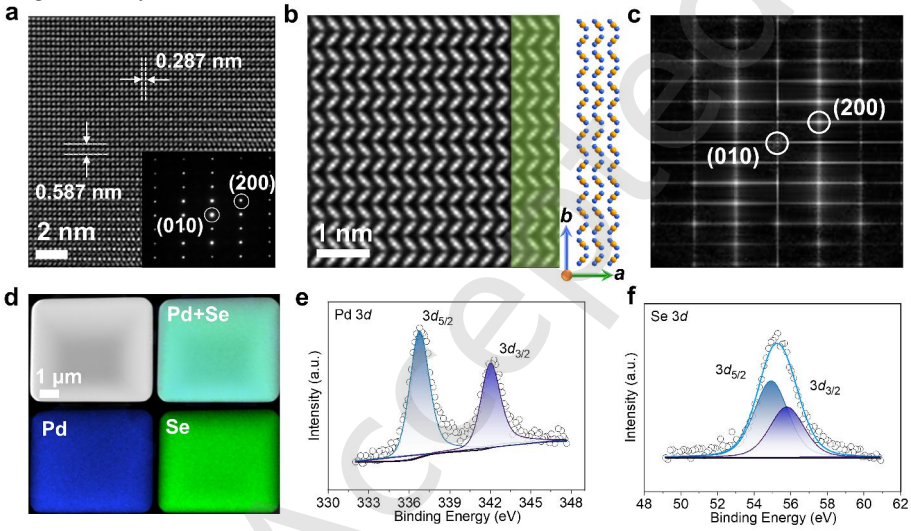

Figure 2. Crystal structure and chemical purity characterization of $PdSe_2$ nanosheets. (a) HRTEM image of a $PdSe_2$ nanosheet, revealing interplanar spacings of 0.287 nm for the (200) plane and 0.587 nm for the (010) plane. The inset shows the corresponding SAED pattern. (b) Atomic-resolution STEM image of the $PdSe_2$ nanosheet viewed along the [001] zone axis (left panel) and the corresponding crystal structure model projected along the *c*-axis (right panel). (c) The corresponding FFT pattern derived from the STEM image. (d) EDS elemental mapping of a $PdSe_2$ nanosheet, indicating the homogeneous distribution of Pd and Se. (e,f) XPS core-level spectra of Pd 3*d* and Se 3*d* for the $PdSe_2$ nanosheets.

The pentagonal $PdSe_2$ crystal adopts an orthorhombic symmetry with lattice parameters a = 0.574 nm, b = 0.586 nm, c = 0.771 nm, and $\alpha = \beta = \gamma = 90°$. The atomic structure of the CVT-grown $PdSe_2$ nanosheets was characterized using transmission electron microscopy (TEM). The high-resolution transmission electron microscopy (HRTEM) image shown in Figure 2a revealed clear lattice fringes with spacings of 0.287 nm and 0.587 nm, which were assigned to the (200) and (010) principal crystal planes of the pentagonal $PdSe_2$ crystal, respectively. The selected area electron diffraction (SAED) pattern exhibited sharp lattice diffraction spots corresponding to the two labeled (200) and (010) planes, confirming the single-crystalline nature of the as-grown $PdSe_2$. Atomic-resolution scanning transmission electron microscopy (STEM) characterization of $PdSe_2$ revealed a periodic atomic arrangement with a boomerang-like pattern along the [001] direction, which matched well with the crystal model viewed from the *c*-axis (Figure 2b). The corresponding fast Fourier transform (FFT) pattern exhibited a set of bright spots arranged in orthorhombic symmetry, characteristic of the $PdSe_2$ lattice (Figure 2c). The scanning TEM energy-dispersive X-ray spectroscopy (STEM-EDS) elemental mapping in Figure 2d demonstrated a homogeneous spatial distribution of Pd and Se elements. In addition, the X-ray diffraction patterns of two batches of CVT-grown $PdSe_2$ nanosheets exhibited a distinct (002) diffraction peak, suggesting preferentially oriented growth of the $PdSe_2$ nanosheets on the substrate (Figure S9). X-ray photoelectron spectroscopy (XPS) analyses were performed to identify the elemental composition and surface chemical bonding states of the sample. As shown in Figures 2e and 2f, two prominent peaks corresponding to the Pd $3d_{3/2}$ and Pd $3d_{5/2}$ orbitals were observed at 342.1 eV and 336.8 eV, with a separation of ≈5.3 eV due to spin-orbit splitting. The Se 3*d* spectrum was fitted with two peaks located at 55.8 eV and 54.9 eV, which were attributed to the binding states of Se $3d_{3/2}$ and Se $3d_{5/2}$, respectively [11]. The absence of other valence states confirmed the chemical purity of the as-grown $PdSe_2$ nanosheets.

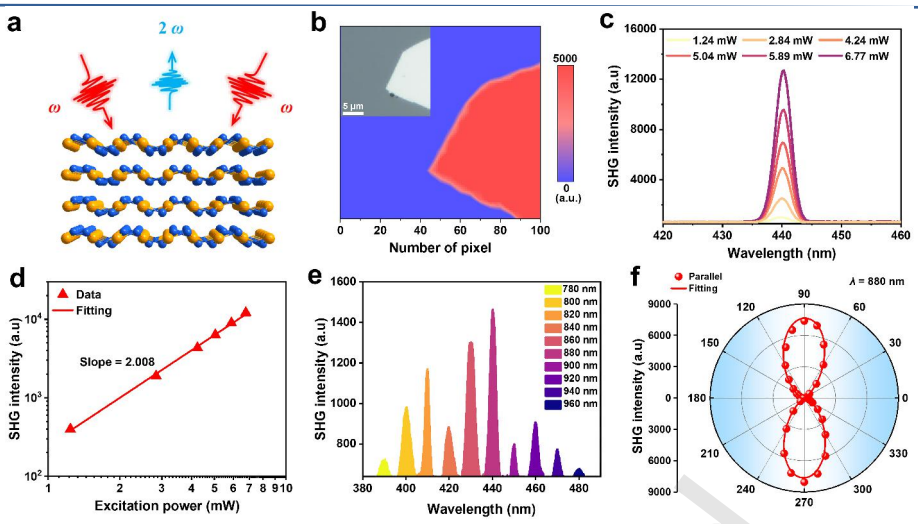

Figure 3. SHG process in few-layer $PdSe_2$. (a) Schematic illustration of the SHG process in 2D $PdSe_2$. (b) Spatial mapping of the integrated SHG signals of a $PdSe_2$ nanosheet. The inset shows the corresponding optical image. (c) SHG spectra of a 6L $PdSe_2$ nanosheet under different laser excitation power (λ = 880 nm). (d) Power dependence of the SHG intensity for 6L $PdSe_2$. (e) SHG spectra of 6L $PdSe_2$ with excitation wavelengths ranging from 780 to 960 nm. (f) Polarization-resolved SHG intensity (red dots) as a function of the polarization angle under 880 nm excitation, along with the fitted curves (solid lines) for 6L $PdSe_2$.

Second-harmonic generation (SHG) activity is a key signature of inversion-symmetry breaking in 2D materials. In contrast to common 2D transition metal dichalcogenides, odd-layer $PdSe_2$ crystals belong to the $P2_1/c$ space group and C_{2h} ($2/m$) point group with inversion symmetry, while even-numbered layers belong to the $Pca2_1$ space group and C_{2v} ($mm2$) point group without inversion symmetry [7, 45]. Therefore, even-layer $PdSe_2$ can exhibit pronounced SHG activity, as illustrated in Figure 3a. The sample used for nonlinear optical measurements had a thickness of 6 layers (6L), as shown in Figure S4a. Figure 3b displays the spatial mapping of the SHG intensity over the $PdSe_2$ sample under an excitation wavelength of 880 nm. The sample exhibited high uniformity in intensity distribution, suggesting the single-crystalline nature of the CVT-grown $PdSe_2$ nanosheet. Figure 3c presents the excitation power-dependent SHG spectra of the 6L $PdSe_2$ sample. An emission peak centered at 440 nm was clearly detected, exactly half the wavelength of the excitation laser. The SHG intensity scaled quadratically with the excitation power and was linearly fitted with a slope of 2.01, confirming the second-order nonlinear process (Figure 3d). Moreover, the SHG intensity of the CVT-grown $PdSe_2$ nanosheet was measured under different excitation wavelengths ranging from 780 to 960 nm in steps of 20 nm at the same excitation power of 3 mW. As shown in Figure 3e, the SHG intensity was strongly dependent on the excitation wavelength and reached a maximum under 880 nm excitation. Furthermore, polarization-resolved SHG signals were collected for the 6L $PdSe_2$ nanosheet under 880 nm excitation with a parallel-polarization configuration. Figure 3f shows the polar plot of the angle-dependent SHG emission of 6L $PdSe_2$ under 880 nm excitation in the parallel-polarization configuration, which exhibited a dumbbell shape with maxima at 90° and minima at 0°. This further confirmed the fundamental anisotropy of the sample, which was in good agreement with mechanically exfoliated counterparts [23, 28].

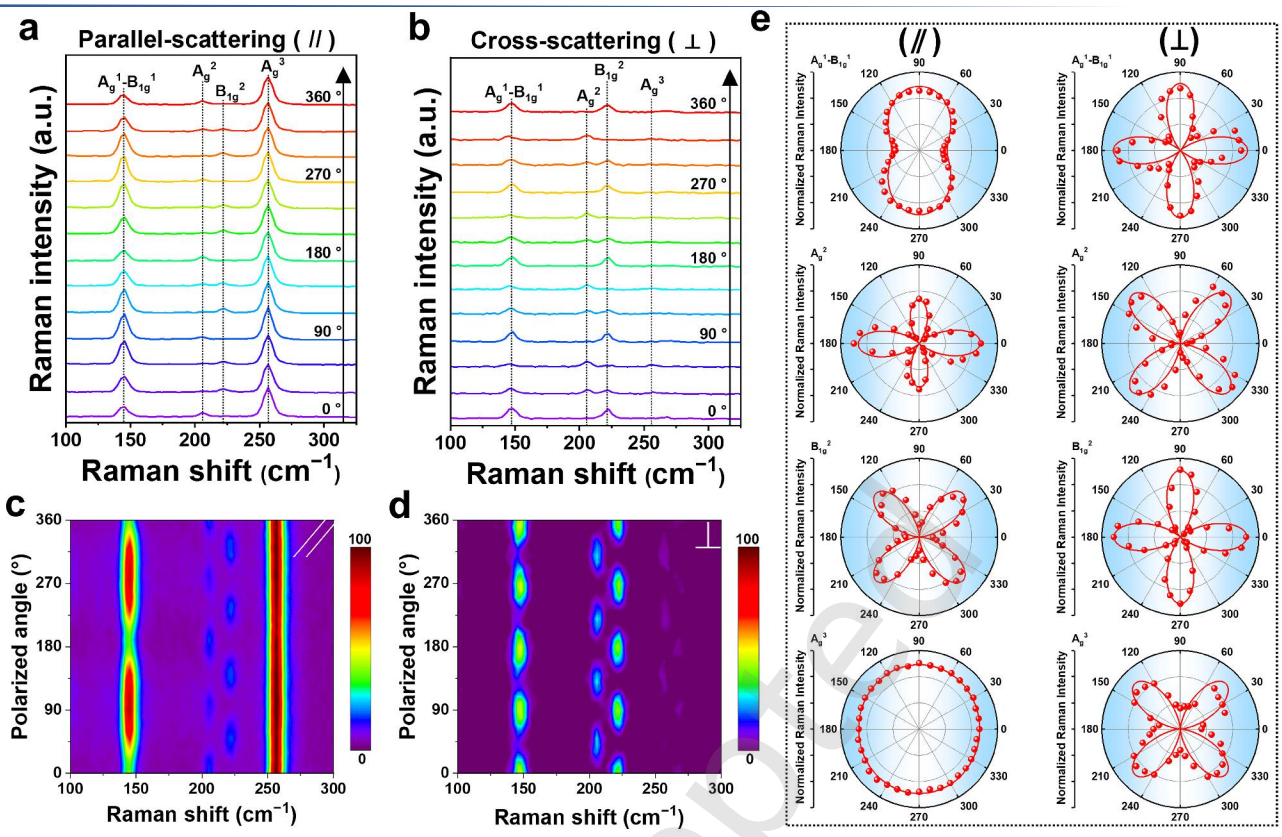

Figure 4. In-plane optical anisotropy of $PdSe_2$ nanosheets. ARPRS of a $PdSe_2$ nanosheet measured with a 532 nm laser under (a) parallel and (b) cross polarization configurations. Contour-color plots of polarized Raman intensity under (c) parallel and (d) cross polarization configurations. (e) Polar plots for the typical Raman modes under parallel and cross polarization configurations. The red dots are experimental data, and the solid lines are the fitting curves.

To investigate the anisotropic vibrational properties of the CVT-grown $PdSe_2$ nanosheets, we performed angle-resolved polarized Raman spectroscopy (ARPRS) under both parallel- and cross-polarization configurations. In our measurements, a half-wave plate was inserted between the filter and the objective, enabling simultaneous adjustment of the polarization of both the incident and scattered light (Figure S10). Figures 4a and 4b show the angle-resolved Raman spectra of the $PdSe_2$ nanosheet as functions of the polarization angle from 0° to 360° under parallel- and cross-polarization configurations, respectively. For these two configurations, the Raman peak intensities of the five vibrational modes (denoted as A_g^1-B_{1g}^1, A_g^2, B_{1g}^2, and A_g^3) exhibited a strong correlation with the polarization angle. The corresponding contour-color maps visualized the periodic modulation of Raman intensity with polarization angle, indicating the intrinsic optical anisotropy of the material (Figures 4c and 4d). To quantitatively analyze the angle-resolved Raman signals, the Raman tensor (R) was used. According to group theory, only A_g and B_{1g} vibrational modes appear in back-scattering Raman measurements [9], and their Raman tensors can be expressed as:

$$R(A_g) = \begin{pmatrix} a & 0 & 0 \\ 0 & b & 0 \\ 0 & 0 & c \end{pmatrix} \quad (1)$$

$$R(B_{1g}) = \begin{pmatrix} 0 & d & 0 \\ d & 0 & 0 \\ 0 & 0 & 0 \end{pmatrix} \quad (2)$$

where a–d represent the amplitudes of each tensor element. The angle-resolved Raman intensity of individual vibrational modes can be quantitatively described by the following formula:

$$I \propto \sum |e_s \cdot R \cdot e_i|^2 \quad (3)$$

where e_s is the polarization vector of the scattered light for parallel or cross polarization ($e_{s//} = [\cos\theta, \sin\theta, 0]$, $e_{s\perp} = [-\sin\theta, \cos\theta, 0]$), e_i is the polarization vector of the incident light ($e_i = [\cos\theta, \sin\theta, 0]^T$), and θ represents the polarization angle determined by rotating the half-wave plate by $\theta/2$ [46]. Therefore, the angle-dependent Raman intensities of A_g and B_{1g} vibrational modes under parallel and cross polarization configurations were given by:

$$I(A_g)^{\parallel} = (a\cos^2\theta + b\sin^2\theta)^2 \quad (4)$$

$$I(A_g)^{\perp} = \left(\frac{b-a}{2}\sin 2\theta\right)^2 \quad (5)$$

$$I(B_{1g})^{\parallel} = (d\sin 2\theta)^2 \quad (6)$$

$$I(B_{1g})^{\perp} = (d\cos 2\theta)^2 \quad (7)$$

Based on the above equations, the Raman scattering intensities were well fitted for each vibrational mode. In the parallel-polarization configuration, the mixed Raman peak (A_g^1-B_{1g}^1) was dominated by the A_g^1 vibrational mode, which exhibited a two-lobed shape with maximum intensity at 90° and 270°, as shown in Figure 4e. Similarly, the other two peaks (A_g^2 and A_g^3)

displayed intensity modulation with a 180° period, with local maxima observed at 90° and 270° or at 0° and 180°. In particular, the direction in which the A_g mode showed the maximum/minimum corresponded to the *a*/*b* crystal axes of $PdSe_2$ [17], enabling the fast identification of crystalline orientations. For the B_{1g}^2 vibrational mode, it showed a four-lobed pattern with a periodic variation of 90°, reaching maximum intensity at 45°, 135°, 225°, and 315°. In the cross-polarization configuration, the mixed Raman peak of A_g^1-B_{1g}^1 became dominated by the B_{1g}^1 vibrational mode. It is worth noting that for this mixed Raman peak, the A_g^1 and B_{1g}^1 modes are very close to each other, making them difficult to distinguish directly in unpolarized Raman spectroscopy. However, using angle-resolved polarized Raman spectroscopy, the peak positions of each Raman mode can be accurately determined based on the different polarization periods of the respective vibrational modes. In this case, all Raman peaks from the A_g and B_{1g} vibrational modes showed a periodic variation of 90°, with the fitted curves exhibiting a four-lobed pattern. Meanwhile, the polarization orientations of the A_g and B_{1g} modes differed by 45°. The angle-dependent Raman intensity modulation of CVT-grown $PdSe_2$ nanosheets arises from the orthorhombic lattice symmetry, where the asymmetric pentagonal rings induce anisotropic polarizability and distinct Raman tensor elements for A_g and B_{1g} vibrational modes, resulting in a strongly polarization-dependent Raman response.

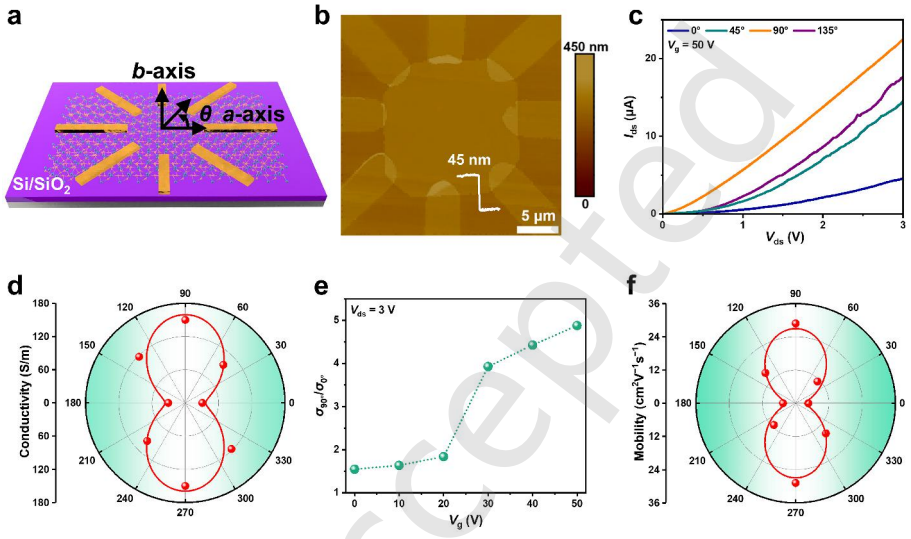

Figure 5. In-plane electrical anisotropy of $PdSe_2$ nanosheets. (a) Schematic representation of the $PdSe_2$ transistor fabricated with eight-terminal electrodes. The direction along the crystallographic *a*-axis was defined as 0°. (b) AFM topography image of the device fabricated on a 45-nm-thick $PdSe_2$ nanosheet. (c) Angle-dependent output curves of the device at V_g = 50 V. (d) Angle-dependent conductivity of the $PdSe_2$ device. (e) Ratio of σ_b/σ_a for the device as a function of gate voltage at V_{ds} = 3 V. (f) Angle-dependent carrier mobility of the device.

Subsequently, angle-resolved electrical transport measurements were performed on $PdSe_2$ nanosheets by fabricating field-effect transistors to reveal their in-plane electrical anisotropy. As illustrated in Figure 5a, eight electrodes were arranged evenly in a circular pattern, with an angle of 45° between adjacent electrodes. The pair of electrodes aligned along the *a*-axis was defined as 0°. The thickness of the $PdSe_2$ nanosheet was measured to be 45 nm based on the AFM image in Figure 5b. Figure 5c shows the output characteristics (I_{ds}–V_{ds}) of the device measured across each diagonal electrode pair at V_g = 50 V, revealing a clear angular dependence. Figure 5d plots the angular variation of electrical conductance (σ) for the device, which was well fitted by the following equation:

$$\sigma(\theta) = \sigma_a cos^2\theta + \sigma_b sin^2\theta \quad (8)$$

where σ_a and σ_b represent the electrical conductivities along the *a*- and *b*-axes, respectively, and θ is defined as the angle measured from the *a*-axis (0°). At V_g = 50 V, the device showed a notable electrical conductivity ratio (σ_b/σ_a) of 4.9. In addition, the angle-dependent conductivity was characterized under various gate voltages (Figure S11a–e). The device displayed gate-tunable electrical anisotropy along with typical *n*-type transport behavior. Specifically, as V_g was reduced from 50 V to 0 V, the σ_b/σ_a ratio gradually decreased to 1.5 (Figure 5e), which can be attributed to the device entering the subthreshold regime at lower gate voltages, leading to an increase in channel resistance. Transfer characteristics (I_{ds}–V_g) of the device were further measured across each diagonal electrode pair, confirming angle-dependent performance (Figure S11f). The electron mobility (μ) of the device was derived from the transfer curves using the following equation:

$$\mu = \frac{L}{W}\frac{d}{\varepsilon_0\varepsilon_r}\frac{1}{V_{ds}}\frac{dI_{ds}}{dV_g} \quad (9)$$

where L and W represent the channel length and width, respectively, $\varepsilon_0 = 8.85 \times 10^{-12}$ F m^{-1} is the vacuum permittivity, ε_r = 3.9 is the relative permittivity of the SiO_2 dielectric layer, and d = 300 nm corresponds to the thickness of the SiO_2 layer. As shown in Figure 5f, the maximum mobility reached 28.8 cm^2 V^{-1} s^{-1} along the *b*-axis, whereas the minimum was 4.6 cm^2 V^{-1} s^{-1} along the *a*-axis, yielding an anisotropic mobility ratio of approximately 6.3. This value was competitive among reported anisotropic 2D semiconductors such as GeSe, PdPS, and black arsenic (Figure S12). The electrical anisotropy can be attributed to the anisotropic effective masses along different crystallographic directions, as reported in previous theoretical studies [47]. The puckered pentagonal structure leads to different orbital overlaps and carrier scattering rates along the *a*-

and *b*-axes of $PdSe_2$, giving rise to the observed directional dependence of electrical conductivity and mobility.

4 Conclusions

In summary, we have demonstrated a growth-parameter-regulated bottom-up CVT route for growing few-layer and multilayer $PdSe_2$ nanosheets on sapphire substrates. By optimizing the growth temperature and substrate selection, we obtained rectangular nanosheets with lateral sizes ranging from 10 to 50 μm and thicknesses from 4 to 55 nm. STEM imaging, SAED patterns, low-frequency Raman spectroscopy, and XRD measurements collectively confirmed the high crystalline quality and the formation of the pentagonal $PdSe_2$ phase in the as-grown products. The $PdSe_2$ nanosheets exhibited intrinsic nonlinear optical properties and strong in-plane optical anisotropy, as revealed by SHG activity and ARPRS. Furthermore, electrical transport measurements on field-effect transistors fabricated with the CVT-grown $PdSe_2$ nanosheets demonstrated pronounced anisotropic ratios of 4.9 for electrical conductivity and 6.3 for carrier mobility. The CVT approach developed here may be extended to other pentagonal 2D materials, paving the way for their future applications in anisotropic electronics and photonics.

Electronic Supplementary Material: Supplementary material, including growth-parameter optimization, optical microscopy and AFM topography images, Raman comparison with mechanically exfoliated nanosheets, ambient-stability characterization, XRD analysis, polarized Raman setup, angle-dependent electrical measurements, and anisotropic mobility comparison, is available in the online version of this article at https://doi.org/10.26599/NR.2026.94909039.

Data availability

All data needed to support the conclusions in the paper are presented in the manuscript and/or the Electronic Supplementary Material. Additional data related to this paper may be requested from the corresponding author upon request.

Acknowledgements

This work was supported by the National Natural Science Foundation of China (NSFC)-Research Grants Council (RGC) of Hong Kong Joint Research Program (Grant No. 62261160574), and other NSFC projects (Grant Nos. 22405176, 62505193), the Guangdong Basic and Applied Basic Research Foundation (Grant No. 2024A1515010295), the China Postdoctoral Science Foundation (CPSF) (Grant Nos. 2024M752105, 2024T170580), and the Postdoctoral Fellowship Program of CPSF (Grant No. GZB20230450).

Declaration of competing interest

All the contributing authors report no conflict of interests in this work.

Author contribution statement

H. L. L. and J. D. L.: Data curation, investigation, validation, formal analysis. D. W. and H. B. G.: Investigation, methodology. J. Z. L. and T. C. H.: Resources, review & editing. Z. H., J. Q. Z., Y. T. S., and J. Q. H.: Methodology, visualization. J. D. L., Q. Y. H., and W. J. Z.: Project administration, supervision, validation, manuscript writing, funding acquisition.

Use of AI statement

None.

References

[1] Li, X.; Liu, H. Y.; Ke, C. M.; Tang, W. Q.; Liu, M. Y.; Huang, F. H.; Wu, Y. P.; Wu, Z. M.; Kang, J. Y. Review of anisotropic 2D materials: controlled growth, optical anisotropy modulation, and photonic applications. *Laser Photonics Rev.* **2021**, *15*, 2100322.

[2] Lin, Z. T.; Yang, X. G.; He, J. D.; Dong, N.; Li, B. J. Structural and optoelectronic characterization of anisotropic two-dimensional materials and applications in polarization-sensitive photodetectors. *Appl. Phys. Rev.* **2025**, *12*, 011301.

[3] Yang, H.; Li, W. H.; Wang, M.; Chen, X. P.; Tan, B. H.; Cheng, Z. W.; Han, C. C.; Huang, Y. Z. 2D AuPS: revealing giant in-plane anisotropy driven by mixed-coordination via stereoscopic distortion. *ACS Nano* **2025**, *19*, 42299–42309.

[4] He, K. X.; Ran, W. H.; Xu, S. D.; Wen, J.; Qiu, S. Q.; Liu, T. W.; Xin, K. Y.; Yu, Y. L.; Liu, D. Y.; Huang, Q. Q.; Shen, G. Z.; Wei, Z. M.; Zhou, Z. Q. Polarization signal amplification of 2D GeSe-based polarization-sensitive photodetectors. *Adv. Mater.* **2025**, *37*, 2509066.

[5] Liu, J. D.; Gan, H. B.; Hao, Q. Y.; Zeng, Y. H.; Gong, Y. N.; Zhu, J. Q.; Huang, J. R.; Liu, F.; Zhang, W. J. High-performance visible and near-infrared dual-band photodetector based on anisotropic 2D NbS_3 with perpendicularly reversed polarization behaviors. *InfoMat* **2025**, *7*, e12625.

[6] Li, P. Y.; Zhang, J. T.; Zhu, C.; Shen, W. F.; Hu, C. G.; Fu, W.; Yan, L.; Zhou, L. J.; Zheng, L.; Lei, H. X.; Liu, Z.; Zhao, W. N.; Gao, P. Q.; Yu, P.; Yang, G. W. Penta-PdPSe: a new 2D pentagonal material with highly in-plane optical, electronic, and optoelectronic anisotropy. *Adv. Mater.* **2021**, *33*, 2102541.

[7] Oyedele, A. D.; Yang, S. Z.; Liang, L. B.; Puretzky, A. A.; Wang, K.; Zhang, J. J.; Yu, P.; Pudasaini, P. R.; Ghosh, A. W.; Liu, Z.; Rouleau, C. M.; Sumpter, B. G.; Chisholm, M. F.; Zhou, W.; Rack, P. D.; Geohegan, D. B.; Xiao, K. $PdSe_2$: pentagonal two-dimensional layers with high air stability for electronics. *J. Am. Chem. Soc.* **2017**, *139*, 14090–14097.

[8] Pi, L. J.; Hu, C. G.; Shen, W. F.; Li, L.; Luo, P.; Hu, X. Z.; Chen, P.; Li, D. Y.; Li, Z. X.; Zhou, X.; Zhai, T. Y. Highly in-plane anisotropic 2D $PdSe_2$ for polarized photodetection with orientation selectivity. *Adv. Funct. Mater.* **2021**, *31*, 2006774.

[9] Yu, J.; Kuang, X. F.; Gao, Y. J.; Wang, Y. P.; Chen, K. Q.; Ding, Z. K.; Liu, J.; Cong, C. X.; He, J.; Liu, Z. W.; Liu, Y. P. Direct observation of the linear dichroism transition in two-dimensional palladium diselenide. *Nano Lett.* **2020**, *20*, 1172–1182.

[10] Xie, C. Y.; Jiang, S. L.; Gao, Y. L.; Hong, M.; Pan, S. Y.; Zhao, J. J.; Zhang, Y. F. Giant thickness-tunable bandgap and robust air stability of 2D palladium diselenide. *Small* **2020**, *16*, 2000754.

[11] Hao, Q. Y.; Huang, J. R.; Liu, J. D.; Li, J. Z.; Gan, H. B.; Tu, Y. D.; Wang, Z. X.; Ou, H. H.; Li, Z. W.; Hu, Y. T.; Zhang, W. J. Controllable phase transformation by van der Waals encapsulation in electrochemically exfoliated $PdSe_2$ nanosheets. *Adv. Funct. Mater.* **2024**, *34*, 2316733.

[12] Yang, Q. S.; Wu, Y. B.; Zhu, L.; Shan, J. J.; Wang, G.; Li, X. X.; Zhao, E. D.; Jiang, S. L.; Shi, X. L.; Chen, Z. G.; Zou, J.; Liang, S. J.; Miao, F.; Zhang, W. Q.; Lin, J. H. Latent phase transition in two-dimensional $PdSe_2$. *Phys. Rev. Lett.* **2025**, *135*, 206102.

[13] Liu, X. W.; Shan, J. J.; Cao, T. J.; Zhu, L.; Ma, J. Y.; Wang, G.; Shi, Z. D.; Yang, Q. S.; Ma, M. Y.; Liu, Z. L.; Yan, S. N.; Wang, L. Z.; Dai, Y. D.; Xiong, J. L.; Chen, F. Q.; Wang, B. W.; Pan, C.; Wang, Z. L.; Cheng, B.; He, Y. M.; Luo, X.; Lin, J. H.; Liang, S. J.; Miao, F. On-device phase engineering. *Nat. Mater.* **2024**, *23*, 1363–1369.

[14] Liu, M. Q.; Cui, T. H.; Feng, J. W.; Wu, Y.; Bi, J. S.; Aierken, A.; Liu, X. F.; Wang, G. G.; Liu, Z. Low-temperature growth of centimeter-sized 2D $PdSe_2$ by self-limiting liquid-phase edge epitaxy. *J. Am. Chem. Soc.* **2025**,

147, 9122–9133.

[15] Gu, Y. Y.; Zhang, L. Z.; Cai, H.; Liang, L. B.; Liu, C. Z.; Hoffman, A.; Yu, Y. L.; Houston, A.; Puretzky, A. A.; Duscher, G.; Rack, P. D.; Rouleau, C. M.; Meng, X. M.; Yoon, M.; Geohegan, D. B.; Xiao, K. Stabilized synthesis of 2D verbeekite: monoclinic $PdSe_2$ crystals with high mobility and in-plane optical and electrical anisotropy. *ACS Nano* **2022**, *16*, 13900–13910.

[16] Wang, J. L.; Peng, Y.; Zhou, T.; Fu, J. T.; Quan, W. Z.; Cheng, Y. J.; Ding, H. X.; Zhang, Y. F. Direct syntheses of 2D noble transition metal dichalcogenides toward electronics, optoelectronics, and electrocatalysis-related applications. *Small* **2025**, *21*, 2407233.

[17] Sierra, J. F.; Světlík, J.; Torres, W. S.; Camosi, L.; Herling, F.; Guillet, T.; Xu, K.; Reparaz, J. S.; Marinova, V.; Dimitrov, D.; Valenzuela, S. O. Room-temperature anisotropic in-plane spin dynamics in graphene induced by $PdSe_2$ proximity. *Nat. Mater.* **2025**, *24*, 876–882.

[18] Li, M. L.; Sun, H. H.; Liu, C. H.; Zhou, J.; Zhang, G.; Zhang, L. F.; Zhao, Y. S. Abnormal thickness-dependent thermal transport in suspended 2D $PdSe_2$. *Small* **2024**, *20*, 2311125.

[19] Slavich, A.; Ermolaev, G.; Pak, N.; Grudinin, D.; Kravtsov, K.; Tatmyshevskiy, M.; Semkin, V.; Syuy, A.; Mazitov, A.; Minnekhanov, A.; Kazantsev, I.; Dyubo, D.; Eghbali, A.; Yakubovsky, D.; Kashchenko, M.; Podobrii, M.; Titova, E.; Melentev, A.; Zhukova, E.; Tselikov, G.; Kruglov, I.; Svintsov, D.; Novikov, S.; Vyshnevyy, A.; Arsenin, A.; Novoselov, K. S.; Volkov, V. Multifunctional van der Waals $PdSe_2$ for light detection, guiding and modulation. *Nat. Commun.* **2025**, *16*, 9201.

[20] Zhang, Y. X.; Tian, H. D.; Li, H. X.; Yoon, C.; Nelson, R. A.; Li, Z. L.; Watanabe, K.; Taniguchi, T.; Smirnov, D.; Kawakami, R. K.; Goldberger, J. E.; Zhang, F.; Lau, C. N. Quantum octets in high mobility pentagonal two-dimensional $PdSe_2$. *Nat. Commun*. **2024**, *15*, 761.

[21] Zhang, R.; Lin, J.; He, T.; Wu, J. F.; Yang, Z. J.; Liu, L. W.; Wen, S. F.; Gong, Y. M.; Lv, H. F.; Zhang, J.; Yin, Y.; Li, F. J.; Lan, C. Y.; Li, C. High-performance piezoresistive sensors based on transfer-free large-area $PdSe_2$ films for human motion and health care monitoring. *InfoMat* **2024**, *6*, e12484.

[22] Gu, Y. Y.; Cai, H.; Dong, J. C.; Yu, Y. L.; Hoffman, A. N.; Liu, C. Z.; Oyedele, A. D.; Lin, Y. C.; Ge, Z. Z.; Puretzky, A. A.; Duscher, G.; Chisholm, M. F.; Rack, P. D.; Rouleau, C. M.; Gai, Z.; Meng, X. M.; Ding, F.; Geohegan, D. B.; Xiao, K. Two-dimensional palladium diselenide with strong in-plane optical anisotropy and high mobility grown by chemical vapor deposition. *Adv. Mater.* **2020**, *32*, 1906238.

[23] Zhang, X.; Deng, Z.; Zhao, L. Y.; Wang, P. Z.; Wang, C. H.; Zhou, L. W.; Wang, G.; Du, T. Y.; Li, M. J. Anomalous in-plane anisotropic harmonic generation in few-layer $PdSe_2$. *ACS Nano* **2025**, *19*, 33557–33566.

[24] Shen, Y. H.; Wang, Q. Pentagon-based 2D materials: classification, properties and applications. *Phys. Rep.* **2022**, *964*, 1–42.

[25] Hou, C. S.; Shen, Y. H.; Wang, Q.; Yoshikawa, A.; Kawazoe, Y.; Jena, P. In-plane sliding ferroelectricity realized in penta-$PdSe_2$/penta-$PtSe_2$ van der Waals heterostructure. *ACS Nano* **2024**, *18*, 16923–16933.

[26] Zhang, C. X.; Chen, Y. Y.; Wang, Q.; Jena, P. Phonon localization and a boson-peak-like anomaly in twisted penta-$PdSe_2$ bilayer. *Nano Lett.* **2025**, *25*, 8689–8695.

[27] Lu, L. S.; Chen, G. H.; Cheng, H. Y.; Chuu, C. P.; Lu, K. C.; Chen, C. H.; Lu, M. Y.; Chuang, T. H.; Wei, D. H.; Chueh, W. C.; Jian, W. B.; Li, M. Y.; Chang, Y. M.; Li, L. J.; Chang, W. H. Layer-dependent and in-plane anisotropic properties of low-temperature synthesized few-layer $PdSe_2$ single crystals. *ACS Nano* **2020**, *14*, 4963–4972.

[28] Yu, J.; Kuang, X. F.; Li, J. Z.; Zhong, J. H.; Zeng, C.; Cao, L. K.; Liu, Z. W.; Zeng, Z. X. S.; Luo, Z. Y.; He, T. C.; Pan, A. L.; Liu, Y. P. Giant nonlinear optical activity in two-dimensional palladium diselenide. *Nat. Commun.* **2021**, *12*, 1083.

[29] Zhong, J. H.; Yu, J.; Cao, L. K.; Zeng, C.; Ding, J. N.; Cong, C. X.; Liu, Z. W.; Liu, Y. P. High-performance polarization-sensitive photodetector based on a few-layered $PdSe_2$ nanosheet. *Nano Res*. **2020**, *13*, 1780–1786.

[30] Dai, M. J.; Wang, C. W.; Ye, M.; Zhu, S.; Han, S.; Sun, F. Y.; Chen, W. D.; Jin, Y. H.; Chua, Y. D.; Wang, Q. J. High-performance, polarization-sensitive, long-wave infrared photodetection via photothermoelectric effect with asymmetric van der Waals contacts. *ACS Nano* **2022**, *16*, 295–305.

[31] Li, G.; Yin, S. Q.; Tan, C. Y.; Chen, L. J.; Yu, M. X.; Li, L.; Yan, F. Fast photothermoelectric response in CVD-grown $PdSe_2$ photodetectors with in-plane anisotropy. *Adv. Funct. Mater*. **2021**, *31*, 2104787.

[32] Irvine, C. T.; Hoefer, N.; Moser, M. J.; Nelson, R. A.; McComb, D. W.; Goldberger, J. E. Diselenide dianion's dual powers: $PdSe_2$ polymorph control and Pd_3Se_{10} superatomic crystal creation. *Chem. Mater.* **2023**, *35*, 4404–4411.

[33] Wang, D. Y.; Luo, F.; Lu, M.; Xie, X. J.; Huang, L.; Huang, W. Chemical vapor transport reactions for synthesizing layered materials and their 2D counterparts. *Small* **2019**, *15*, 1804404.

[34] Wang, J. Y.; Zheng, H. S.; Xu, G. C.; Sun, L. F.; Hu, D. K.; Lu, Z. X.; Liu, L. N.; Zheng, J. Y.; Tao, C. G.; Jiao, L. Y. Controlled synthesis of two-dimensional 1T-$TiSe_2$ with charge density wave transition by chemical vapor transport. *J. Am. Chem. Soc*. **2016**, *138*, 16216–16219.

[35] Hu, D. K.; Xu, G. C.; Xing, L.; Yan, X. X.; Wang, J. Y.; Zheng, J. Y.; Lu, Z. X.; Wang, P.; Pan, X. Q.; Jiao, L. Y. Two-dimensional semiconductors grown by chemical vapor transport. *Angew. Chem., Int. Ed.* **2017**, *56*, 3611–3615.

[36] Hu, D. K.; Zhao, T. Q.; Ping, X. F.; Zheng, H. S.; Xing, L.; Liu, X. Z.; Zheng, J. Y.; Sun, L. F.; Gu, L.; Tao, C. G.; Wang, D.; Jiao, L. Y. Unveiling the layer-dependent catalytic activity of $PtSe_2$ atomic crystals for the hydrogen evolution reaction. *Angew. Chem., Int. Ed.* **2019**, *58*, 6977–6981.

[37] Sun, Z. J.; Chen, W. J.; Zhang, B. W.; Gao, L.; Tao, K. Z.; Li, Q.; Sun, J. L.; Yan, Q. F. Polarization conversion in bottom-up grown quasi-1D fibrous red phosphorus flakes. *Nat. Commun*. **2023**, *14*, 4398.

[38] Xing, L.; Yan, X. X.; Zheng, J. Y.; Xu, G. C.; Lu, Z. X.; Liu, L. N.; Wang, J. H.; Wang, P.; Pan, X. Q.; Jiao, L. Y. Highly crystalline $ReSe_2$ atomic layers synthesized by chemical vapor transport. *InfoMat* **2019**, *1*, 552–558.

[39] Zhao, X. X.; Shi, J. W.; Yin, Q.; Dong, Z.; Zhang, Y.; Kang, L. X.; Yu, Q.; Chen, C.; Li, J.; Liu, X. F.; Zhang, K. Controllable synthesis of high-quality two-dimensional tellurium by a facile chemical vapor transport strategy. *iScience* **2022**, *25*, 103594.

[40] Ma, Z.; Ren, C. X.; Wu, Y.; Qiu, H. L.; Liu, H. J.; Hu, Z. G.; Wu, Y. C. Dopant-induced giant photoluminescence of monolayer MoS_2 by chemical vapor transport. *Adv. Mater. Interfaces* **2022**, *9*, 2200431.

[41] Zhao, B. J.; Chen, Q. B.; An, Y. K.; Liu, H. J.; Qiu, H. L.; Liu, M.; Hu, Z. G.; Wu, Y. C. Photoluminescence behaviors of 2D-$Cs_3Bi_2I_9$/2D-MoS_2 vertical heterostructures prepared by the one-step CVT growth method. *ACS Appl. Opt. Mater*. **2024**, *2*, 2294–2301.

[42] Chen, Y.; Liu, M. Y.; Luo, S.; Wan, P.; Liu, D. Y.; Shen, D. Y.; Li, J.; Li, B.; Wu, H.; Wu, R. X.; Duan, X. D. Synthesis of two-dimensional MoS_2 and WS_2 films by enclosed chemical vapor transport method below the back-end-of-line temperature. *Nano Lett.* **2026**, *26*, 222–230.

[43] Puretzky, A. A.; Oyedele, A. D.; Xiao, K.; Haglund, A. V.; Sumpter, B. G.; Mandrus, D.; Geohegan, D. B.; Liang, L. B. Anomalous interlayer vibrations in strongly coupled layered $PdSe_2$. *2D Mater.* **2018**, *5*, 035016.

[44] Ding, J. N.; Xie, X.; Ouyang, X. Y.; Chen, J. Y.; Ouyang, F. P.; Liu, Z. W.; Wang, J. T.; He, J.; Liu, Y. P. Pressure-driven layer-dependent phase transitions and enhanced interlayer coupling in $PdSe_2$ crystals. *Nano Res.* **2024**, *17*, 10170–10178.

[45] Zhu, S.; Duan, R. H.; Xu, X. D.; Sun, F. Y.; Chen, W. D.; Wang, F. K.; Li, S. Y.; Ye, M.; Zhou, X.; Cheng, J. L.; Wu, Y.; Liang, H. K.; Kono, J.; Li, X. J.; Liu, Z.; Wang, Q. J. Strong nonlinear optical processes with extraordinary polarization anisotropy in inversion-symmetry broken two-

dimensional PdPSe. *Light Sci. Appl*. **2024**, *13*, 119.
[46] Krahne, R.; Lin, M. L.; Tan, P. H. Interplay of phonon directionality and emission polarization in two-dimensional layered metal halide perovskites. *Acc. Chem. Res*. **2024**, *57*, 2476–2489.
[47] Qin, D.; Yan, P.; Ding, G. Q.; Ge, X. J.; Song, H. Y.; Gao, G. Y. Monolayer $PdSe_2$: a promising two-dimensional thermoelectric material. *Sci. Rep*. **2018**, *8*, 2764.

Electronic Supplementary Material

Chemical vapor transport synthesis of 2D pentagonal $PdSe_2$ with in-plane optical and electrical anisotropy

Haolin Liu[1,§], Jidong Liu[1,§], Di Wu[2], Junzi Li[3], Haibo Gan[1], Zhen He[1], Jiaqi Zhu[4], Yuting Sun[1], Junqi He[1], Tingchao He[3], Qiaoyan Hao[1] ✉, and Wenjing Zhang[1] ✉

[1] *State Key Laboratory of Radio Frequency Heterogeneous Integration, International Collaborative Laboratory of 2D Materials for Optoelectronics Science and Technology of Ministry of Education, Institute of Microscale Optoelectronics, Shenzhen University, Shenzhen 518060, China*

[2] *College of Electronic Engineering, Huainan Normal University, Huainan 232038, China*

[3] *Key Laboratory of Optoelectronic Devices and Systems of Ministry of Education and Guangdong Province, College of Physics and Optoelectronic Engineering, Shenzhen University, Shenzhen 518060, China*

[4] *Institute of Advanced Photonics Technology, Key Laboratory of Photonic Technology for Integrated Sensing and Communication of Ministry of Education, School of Information Engineering, Guangdong University of Technology, Guangzhou 510006, China*

[§]*Haolin Liu and Jidong Liu contributed equally to this work.*

✉Address correspondence to Qiaoyan Hao, hqy@szu.edu.cn; Wenjing Zhang, wjzhang@szu.edu.cn

Supporting information to https://doi.org/10.26599/NR.2026.94909039

Optimization of the growth parameters

1) Growth temperature

The growth temperature played a critical role in determining the number of layers and lateral size of the $PdSe_2$ nanosheets, as shown in Figure S1. At a lower growth temperature of 750 ℃, smaller $PdSe_2$ nanosheets with a higher density were obtained. In contrast, when the temperature was increased to 850 ℃, the density of nanosheets on the substrate decreased significantly. On the *c*-plane sapphire substrate, the optimal growth temperature for $PdSe_2$ was approximately 800 ℃.

2) Substrate

We also investigated the influence of different growth substrates, including SiO_2/Si, mica, and sapphire, on the formation of $PdSe_2$ nanosheets. At a growth temperature of 800 ℃, thin rectangular nanosheets were produced on SiO_2/Si substrates (Figure S2a). However, no characteristic Raman peaks corresponding to pentagonal $PdSe_2$ were observed, indicating poor crystalline quality (Figure S2c). For mica substrates, the Raman spectrum confirmed the presence of the target product, but the resulting nanosheets exhibited a lateral size of less than 10 μm and a thickness exceeding 100 nm under identical growth conditions (Figures S2b and S2d). Among the substrates selected, sapphire proved to be the most suitable for growing 2D pentagonal $PdSe_2$ nanosheets with variable thicknesses.

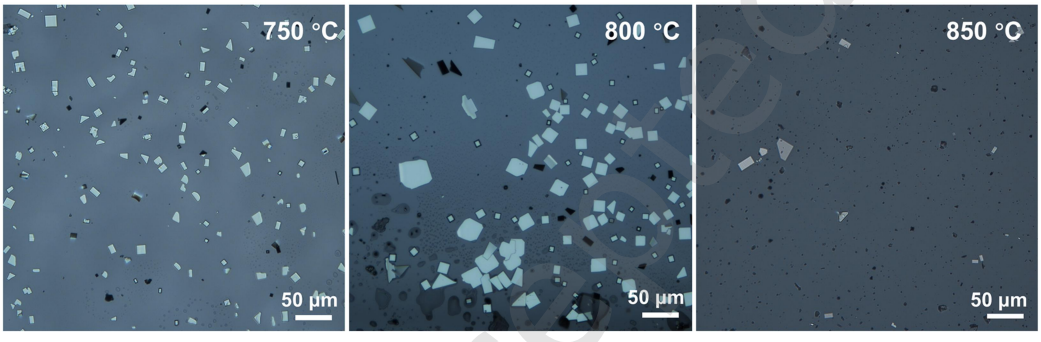

Figure S1**.** Optical microscopy images of $PdSe_2$ nanosheets obtained on sapphire substrates at different growth temperatures.

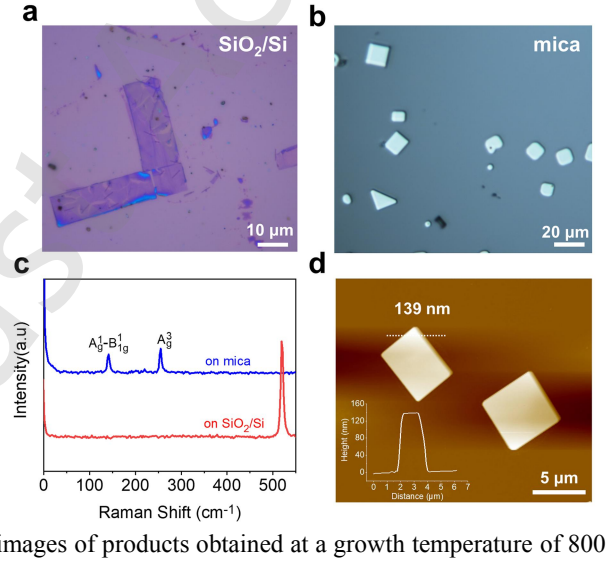

Figure S2**.** (a,b) Optical microscopy images of products obtained at a growth temperature of 800 ℃ on SiO_2/Si and mica substrates. (c) Raman spectra of the products on SiO_2/Si and mica substrates. (d) AFM topography image of the $PdSe_2$ nanosheet grown on a mica substrate.

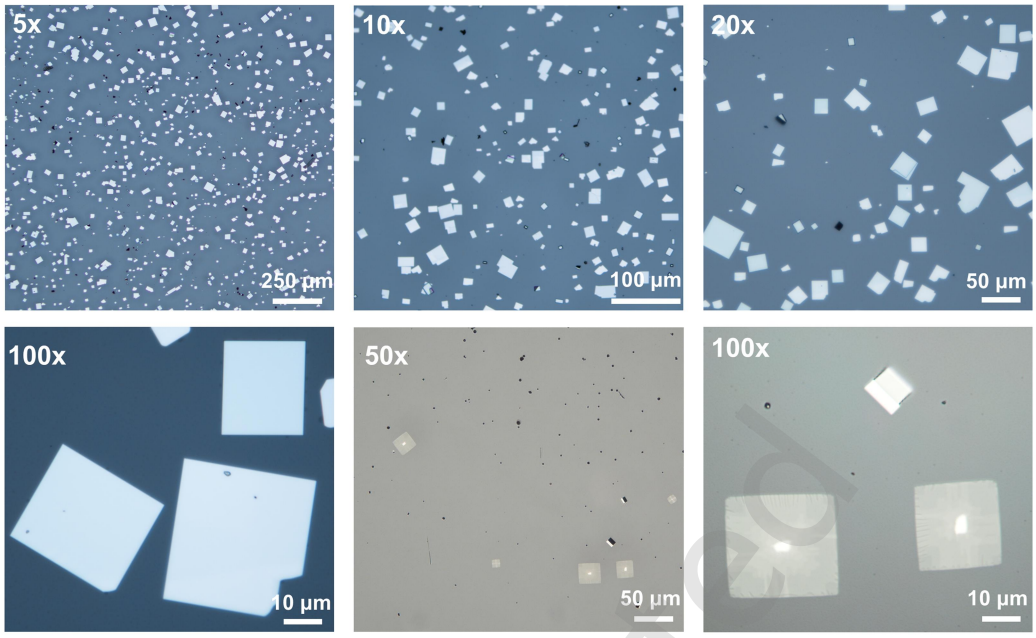

Figure S3**.** Optical microscopy images of $PdSe_2$ nanosheets on sapphire substrates obtained at a growth temperature of 800 ℃.

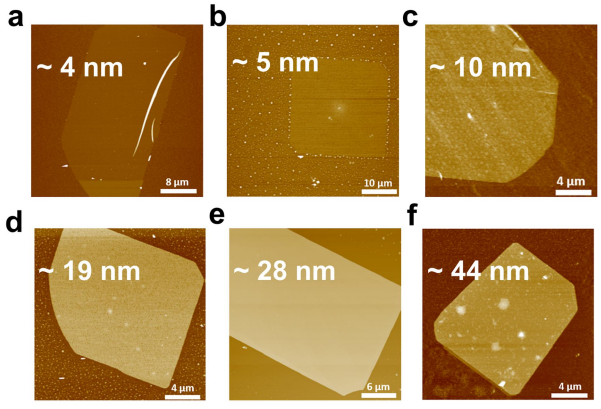

Figure S4. AFM topography images of the as-grown $PdSe_2$ nanosheets with variable thicknesses.

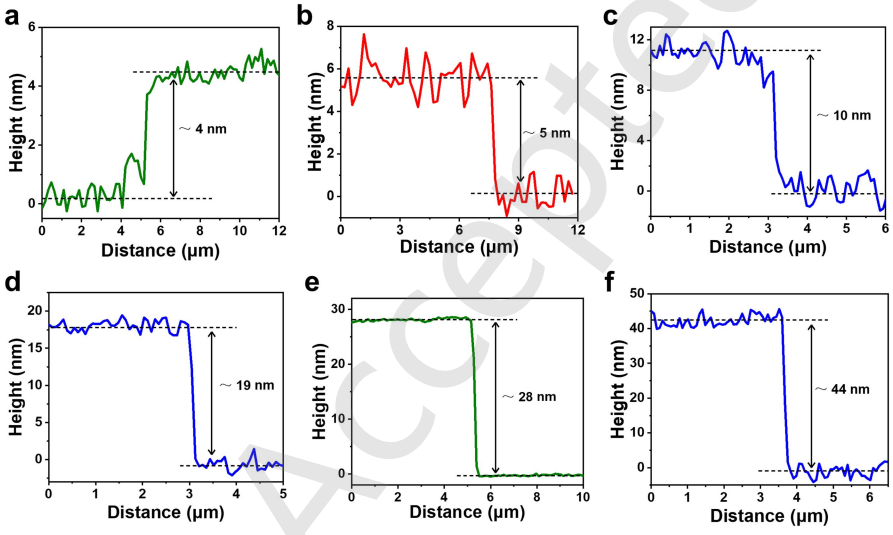

Figure S5. Corresponding height profiles of the as-grown $PdSe_2$ nanosheets in Figure S4.

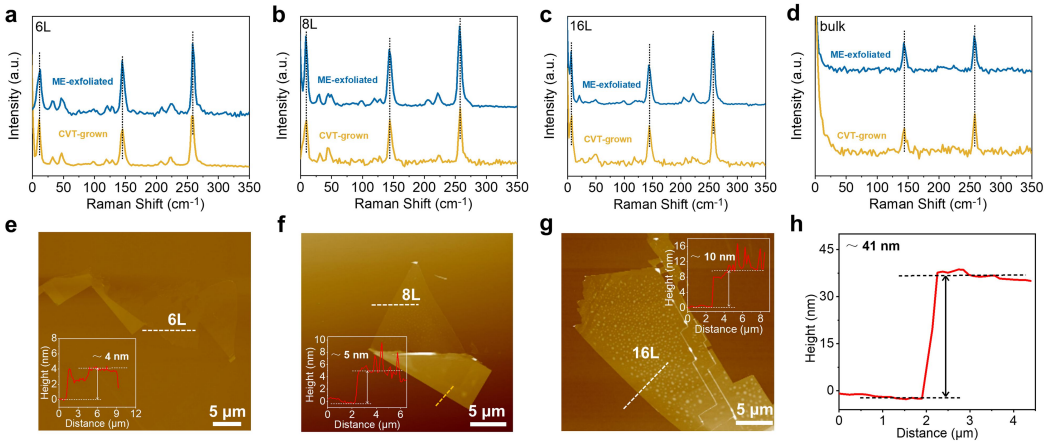

Figure S6. (a–d) Comparison of Raman spectra between CVT-grown $PdSe_2$ nanosheets and mechanically exfoliated (ME) $PdSe_2$ nanosheets with different thicknesses. (e–h) AFM images of the ME-exfoliated samples and the corresponding height profiles along the white lines. The height profile in (h) was extracted along the orange line in (f).

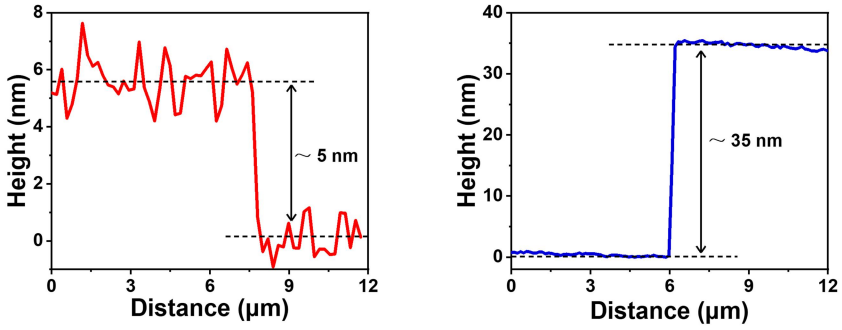

Figure S7. Corresponding height profiles of the as-grown $PdSe_2$ nanosheets shown in Figures 1e and 1g.

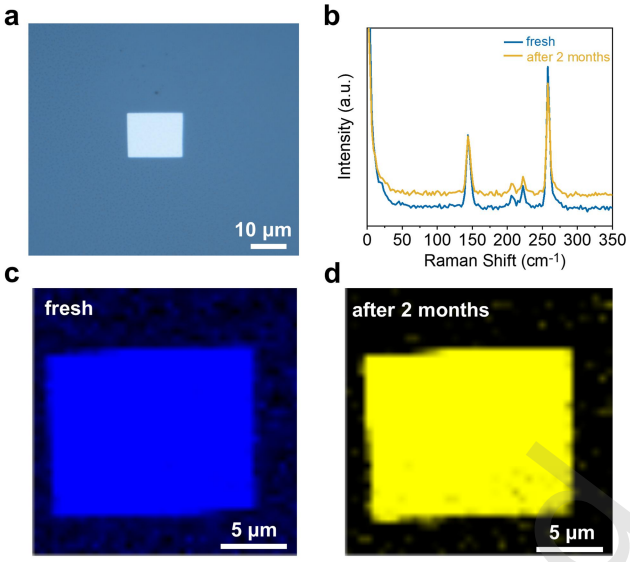

Figure S8. Raman spectra and Raman intensity maps of the A_g^3 peak collected from a CVT-grown $PdSe_2$ nanosheet after two months of ambient exposure.

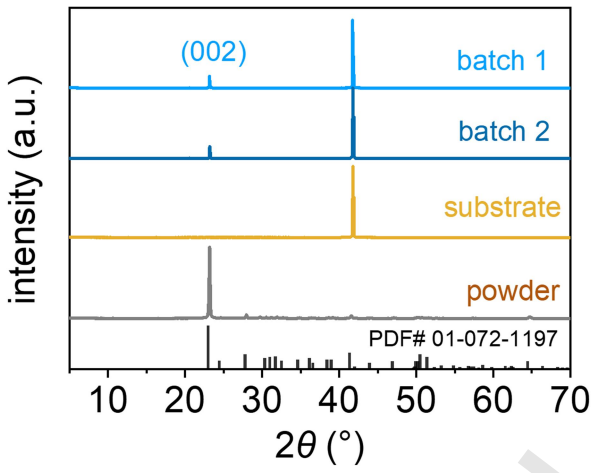

Figure S9. XRD patterns of two batches of CVT-grown $PdSe_2$ nanosheets and $PdSe_2$ powder for comparison.

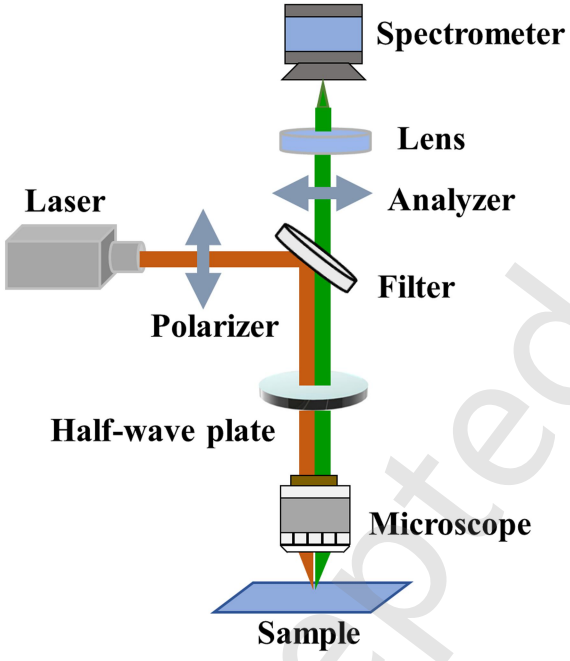

Figure S10**.** Schematic illustration of polarized Raman spectroscopy measurements.

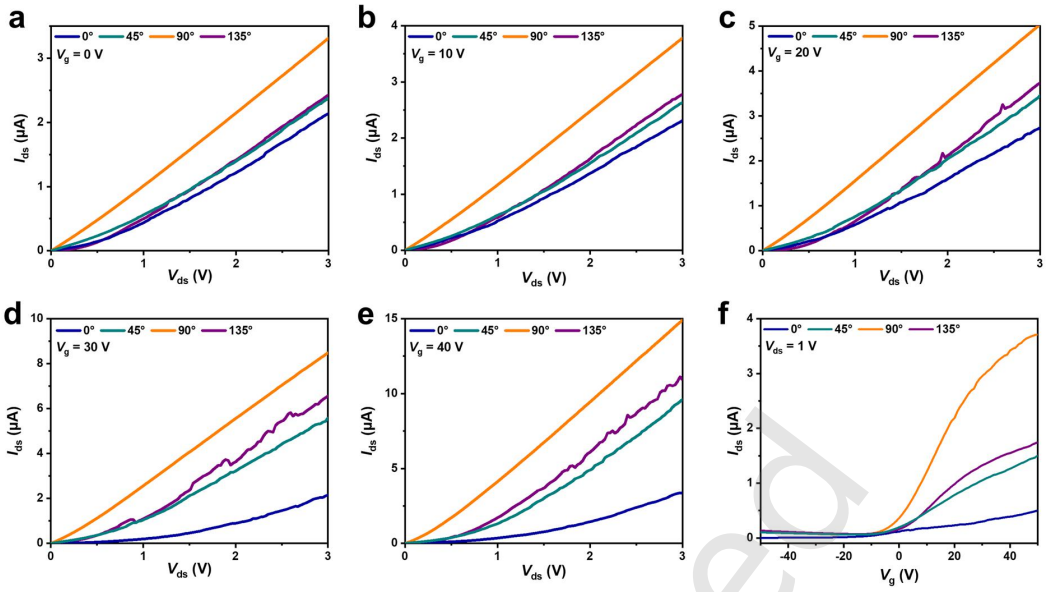

Figure S11. (a−e) Angle-dependent output curves (I_{ds}–V_{ds}) of the $PdSe_2$ nanosheet device under different gate voltages. (f) Angle-resolved transfer curves (I_{ds}–V_g) of the device at V_{ds} = 1 V.

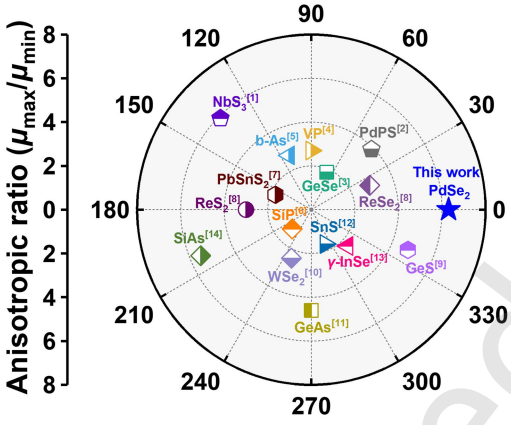

Figure S12. Comparison of anisotropic mobility ratios for transistors based on various low-symmetry 2D materials.

References

[1] Liu, J. D.; Gan, H. B.; Hao, Q. Y.; Zeng, Y. H.; Gong, Y. N.; Zhu, J. Q.; Huang, J. R.; Liu, F.; Zhang, W. J. High-performance visible and near-infrared dual-band photodetector based on anisotropic 2D NbS_3 with perpendicularly reversed polarization behaviors. *InfoMat* **2025**, *7*, e12625.

[2] Duan, R. H.; He, Y. C.; Zhu, C.; Wang, X. W.; Zhu, C.; Zhao, X. X.; Zhang, Z. H.; Zeng, Q. S.; Deng, Y.; Xu, M. Z.; Liu, Z. 2D Cairo pentagonal PdPS: air-stable anisotropic ternary semiconductor with high optoelectronic performance. *Adv. Funct. Mater.* **2022**, *32*, 2113255.

[3] Zhou, X.; Hu, X. Z.; Jin, B.; Yu, J.; Liu, K. L.; Li, H. Q.; Zhai, T. Y. Highly anisotropic GeSe nanosheets for phototransistors with ultrahigh photoresponsivity. *Adv. Sci.* **2018**, *5*, 1800478.

[4] Liu, H. W.; Zhu, C. G.; Chen, Y.; Yi, X.; Sun, X. X.; Liu, Y.; Wang, H.; Wu, G. C.; Wu, J. X.; Li, Y.; Zhu, X. L.; Li, D.; Pan, A. L. Polarization-sensitive photodetectors based on highly in-plane anisotropic violet phosphorus with large dichroic ratio. *Adv. Funct. Mater.* **2024**, *34*, 2314838.

[5] Zhong, M. Z.; Meng, H. T.; Liu, S. J.; Yang, H.; Shen, W. F.; Hu, C. G.; Yang, J. H.; Ren, Z. H.; Li, B.; Liu, Y. Y.; He, J.; Xia, Q. L.; Li, J. B.; Wei, Z. M. In-plane optical and electrical anisotropy of 2D black arsenic. *ACS Nano* **2021**, *15*, 1701–1709.

[6] Hou, S. J.; Guo, Z. F.; Xiong, T.; Wang, X. G.; Yang, J. H.; Liu, Y. Y.; Niu, Z. C.; Liu, S. Y.; Liu, B.; Zhai, S. Q.; Gu, H. G.; Wei, Z. M. Optical and electronic anisotropy of a 2D semiconductor SiP. *Nano Res.* **2022**, *15*, 8579–8586.

[7] Shu, Z. W.; Huang, P.; Peng, Q. J.; Xu, Z.; Suleiman, A. A.; Zhang, X. W.; Bai, X. D.; Zhou, X.; Zhai, T. Y. Growth of ultrathin ternary teallite ($PbSnS_2$) flakes for highly anisotropic optoelectronics. *Matter* **2020**, *2*, 977–987.

[8] Wen, W.; Zhu, Y. M.; Liu, X. L.; Hsu, H.-P.; Fei, Z.; Chen, Y. F.; Wang, X. S.; Zhang, M.; Lin, K.-H.; Huang, F.-S.; Wang, Y.-P.; Huang, Y.-S.; Ho, C.-H.; Tan, P.-H.; Jin, C. H.; Xie, L. M. Anisotropic spectroscopy and electrical properties of 2D $ReS_{2(1-x)}Se_{2x}$ alloys with distorted 1T structure. *Small* **2017**, *13*, 1603788.

[9] Chen, Z. F.; Hwang, W.; Cho, M.; Hoang, A. T.; Kim, M.; Kim, D. W.; Kim, D. H.; Kim, Y. D.; Kim, H. J.; Ahn, J. H.; Soon, A.; Choi, H. J. In-plane optical and electrical anisotropy in low-symmetry layered GeS microribbons. *NPG Asia Mater.* **2022**, *14*, 41.

[10] Chen, P.; Pan, J. B.; Gao, W. C.; Wan, B. S.; Kong, X. H.; Cheng, Y.; Liu, K. H.; Du, S. X.; Ji, W.; Pan, C. F.; Wang, Z. L. Anisotropic carrier mobility from 2H WSe_2. *Adv. Mater.* **2022**, *34*, 2108615.

[11] Yang, S. X.; Yang, Y. H.; Wu, M. H.; Hu, C. G.; Shen, W. F.; Gong, Y. J.; Huang, L.; Jiang, C. B.; Zhang, Y. Z.; Ajayan, P. M. Highly in-plane optical and electrical anisotropy of 2D germanium arsenide. *Adv. Funct. Mater.* **2018**, *28*, 1707379.

[12] Tian, Z.; Guo, C. L.; Zhao, M. X.; Li, R. R.; Xue, J. M. Two-dimensional SnS: a phosphorene analogue with strong in-plane electronic anisotropy. *ACS Nano* **2017**, *11*, 2219–2226.

[13] Pan, Y.; Zhao, Q. X.; Gao, F.; Dai, M. J.; Gao, W.; Zheng, T.; Su, S. C.; Li, J. B.; Chen, H. Y. Strong in-plane optical and electrical anisotropies of multilayered γ-InSe for high-responsivity polarization-sensitive photodetectors. *ACS Appl. Mater. Interfaces* **2022**, *14*, 21383–21391.

[14] Kim, D.; Park, K.; Lee, J. H.; Kwon, I. S.; Kwak, I. H.; Park, J. Anisotropic 2D SiAs for high-performance UV-visible photodetectors. *Small* **2021**, *17*, 2006310.